Title: Spatiotemporally programmable surfaces via viscoelastic shell snapping

Yuzhen Chen, Tianzhen Liu and Lihua Jin*

Yuzhen Chen, Lihua Jin

Department of Mechanical and Aerospace Engineering, University of California, Los

Angeles, Los Angeles, CA 90095, USA

E-mail: lihuajin@seas.ucla.edu

Tianzhen Liu

Key Laboratory of C & PC Structures of Ministry of Education, National Prestress

Engineering Research Center, Southeast University, Nanjing 210096, China

Department of Mechanical and Aerospace Engineering, University of California, Los

Angeles, Los Angeles, CA 90095, USA

Keywords: spatiotemporal programming, textural morphing, reconfigurable, viscoelastic shell,

pseudo-bistability, pneumatic actuation

Abstract:

Many species can dynamically alter their skin textures to enhance their motility and

survivability. Despite the enormous efforts on designing bio-inspired materials with tunable

surface textures, developing spatiotemporally programmable and reconfigurable textural

morphing without complex control remains challenging. Here we propose a design strategy to

achieve surfaces with such properties. The surfaces comprise an array of unit cells with broadly

tailored temporal responses. By arranging the unit cells differently, the surfaces can exhibit

various spatiotemporal responses, which can be easily reconfigured by disassembling and

rearranging the unit cells. Specifically, we adopt viscoelastic shells as the unit cells, which can

be pneumatically actuated to a concave state, and recover the initial convex state some time

1

after the load is removed. We computationally and experimentally show that the recovery time can be widely tuned by the geometry and material viscoelasticity of the shells. By assembling such shells with different recovery time, we build surfaces with pre-programmed spatiotemporal textural morphing under simple pneumatic actuation, and demonstrate temporal evolution of patterns, such as digit numbers and emoji, and spatiotemporal control of friction. This work opens up new avenues in designing spatiotemporal morphing surfaces that could be employed for programming mechanical, optical and electrical properties.

1. Introduction

A lot of living creatures can dynamically adapt their skin textures for locomotion, signaling, and camouflage. For instance, snakes can actively tilt the ventral scales on their skin to prevent sliding when they climb across a complex terrain^[1]. As the masters of camouflage, cephalopods are capable of adaptively altering the morphology of skin papillae against the everchanging background when they move on the seabed^[2,3]. These examples have inspired numerous artificial materials and devices with tunable surface textures for a wide range of applications in aerospace^[4,5], human computer interaction^[6–8], and soft robotics^[9–15]. The actuation for textural morphing relies on either mechanical loads^[4–10,16–20] or embedded stimuli-responsive materials^[13–15,21–28].

Unlike the dynamic textural morphing in nature, most synthetic materials transform into only one targeted surface texture in response to a stimulus. Achieving temporally evolving textures, however, is challenging because it is essential to control the surface in both space and time. A straightforward approach for spatiotemporally programmable textural morphing is utilizing mechatronic systems comprising power supplies, multiple motors or pumps, and electronic control devices ^[7,9,13,14]. Properly programming the actuation of multiple motors and

pumps by an electronic controller can allow one to achieve desired spatiotemporal texture morphing. However, excessive electric and electronic components make the whole system complex, and thus less robust. An alternative approach is directly embedding spatiotemporal control into materials by spatially patterning active materials with different temporal responses to defined stimuli^[14,21,26–28]. However, the temporal texture evolution is unchangeable once the materials have been made. The design of spatiotemporally programmable textural morphing that can be easily operated, controlled and reconfigured on demand is still in its infancy.

Here, we develop a spatiotemporally programmable and reconfigurable surface that can achieve time-dependent textural morphing under simple control. The design of this surface requires unit cells with widely tunable temporal responses under a defined stimulus. These unit cells can be assembled into a surface with a desired spatiotemporal response. The created surface can be easily reconfigured into a new one with different spatiotemporal responses by disassembling and reorganizing the unit cells. One example of such unit cells that we adopt here is a viscoelastic shell which can have convex and concave states (**Figure 1b**), analogous to the extended and retracted states of the papillae on cephalopods' skin (Figure 1a). The shell can buckle into the concave state when subjected to a pressure load, and recovers the convex state after a certain amount of time when the load is removed^[29–33]. The recovery time can be widely tuned by the geometry and viscoelasticity of the shell^[31]. As a result, a surface comprising the shell units with different recovery time can exhibit pre-programmed temporal texture evolution, which can be easily reconfigured by rearranging the shell units (Figure 1c-d). The proposed surfaces are used to display temporal evolution of patterns, such as digit numbers and emoji, and programmed spatiotemporal friction control.

2. Results and Discussion

2.1 Design of viscoelastic shells with tunable recovery time

Consider viscoelastic shells of revolution with the following profile of the internal surfaces (Figure 2a)

$$h(r) = (H - d) \left[1 - 10 \left(\frac{r}{R} \right)^3 + 15 \left(\frac{r}{R} \right)^4 - 6 \left(\frac{r}{R} \right)^5 \right], r \in [0, R], \tag{1}$$

where H is the height, d is the thickness, and R is the radius of the shell. Such geometry ensures dh/dr = 0 and $d^2h/dr^2 = 0$ at both the center (r = 0) and the edge (r = R) of the shell to facilitate the implementation of the boundary conditions in both simulations and experiments. Subjected to clamped boundary conditions and a pressure load Δp , the shell can buckle into a concave shape (dashed lines), yielding a displacement w at its center.

We first conducted finite element analyses (FEA) to study the viscoelastic responses of such shells upon pressure loads using the commercial package Abaqus/Standard (Method). The instantaneous constitutive behavior of the shells is modeled as an incompressible neo-Hookean material with the instantaneous shear modulus μ_0 (Supplementary Text 1). The relaxation of the shear modulus over time t, $\mu(t)$ is described by the Prony series,

$$\mu(t) = \mu_0 \left[1 - \sum_{i=1}^n g_i \left(1 - e^{-t/\tau_i} \right) \right],\tag{2}$$

where n is the number of the series terms, g_i is the dimensionless relaxation modulus, and τ_i is the relaxation time constant. Only the first term of the Prony series is considered in the FEA with the relaxation parameter g and relaxation time constant τ .

We first investigate the instantaneous responses the shells. The normalized pressure $\Delta p/\mu_0$ increases, decreases, and increases again with the normalized displacement w/H for the shells with H/R = 0.4 and different d/R ranging from 0.105 to 0.16 (Figure 2b). We find that the $\Delta p/\mu_0$ -w/H curves for thick shells with $d/R \ge 0.11$ stay above the horizontal line of zero pressure, indicating that these shells are monostable. As d/R decreases below 0.11 (d/R = 0.105), the $\Delta p/\mu_0$ -w/H curves intersect with the horizontal line of zero pressure, indicating that the shells are bistable. The monostable shells can instantaneously recover from their concave shapes once

the pressure load is removed, whereas the bistable shells can stay concave without a pressure load.

Monostable viscoelastic shells are capable of temporarily staying concave for a certain amount of time before recovering to their convex state, even though the pressure load is removed. This phenomenon is called pseudo-bistability^[30–33], and will be utilized to build surfaces with programmable spatiotemporal textural morphing. To quantify the phenomenon in FEA, we instantaneously imposed a pressure load $\Delta p/\mu_0 = 0.03$ on a viscoelastic shell with H/R = 0.4, d/R = 0.11, and g = 0.2, and released the pressure after holding it for 2τ (Figure 2c). The corresponding displacement w-time t relation was computed. As a result, the shell immediately snaps into a concave shape once the pressure is applied, and creeps with a small displacement increase w/H = 0.0326 for $t_{\rm creep} = 2\tau$ during the loading. As the pressure is removed, the shell temporarily stays concave for $t_{\rm rec}/\tau = 7.1$ with w/H slightly decreasing prior to snapping back to the convex state (Figure 2c).

Next, we investigate the effect of loading history, geometry and viscoelasticity on the recovery time t_{rec}/τ . As a result, for the shell with H/R=0.4 subjected to a step pressure load $\Delta p/\mu_0=0.03$, t_{rec}/τ increases with t_{creep}/τ , and saturates when $t_{\text{creep}}/\tau=2$ for a range of d/R and g (Figure 2d). For a given t_{creep}/τ , a larger g leads to a longer t_{rec}/τ . We also find that t_{rec}/τ is considerably reduced when the shell becomes thicker (Figure 2d). These trends can be seen more clearly in the contour plot of t_{rec}/τ with respect to d/R and g when $t_{\text{creep}}/\tau=2$ (Figure 2e); t_{rec}/τ increases as g increases or d/R decreases. The growth rate of t_{rec}/τ with respect to g is dramatically increased as d/R approaches 0.11, which is the boundary demarcating the monostable and bistable shells. The shells corresponding to the region underneath the white line in this contour have a zero recovery time, indicating that they snap back immediately once

the pressure load is removed. We note that $\Delta p/\mu_0$ can increase $t_{\rm rec}/\tau$, but this increase is negligible compared to the effects of $t_{\rm creep}/\tau$, g and d/R (Figure S2).

2.2 Spatiotemporally programmable surfaces and experimental characterization

Having identified how the recovery time is tuned by the loading history, geometry and viscoelasticity, we now demonstrate the spatiotemporally programmable surfaces composed of viscoelastic shells with different recovery time.

We selected two materials that have similar moduli but very different viscoelastic properties for the fabrication: silicone rubber (Dragon SkinTM 30, D30) and urethane rubber (VytaFlexTM 20, V20). We conducted stress relaxation tests for these two rubbers and fitted the two-term Prony series to the data, the results of which are given in **Table 1** (Method and Supplementary Text 1). We find that the silicone rubber D30 is highly hyperelastic whereas the urethane rubber V20 is highly viscoelastic, since their moduli decay by $g_1 + g_2 = 5.08\%$ and 36.71%, respectively, as time approaches infinity. The two terms in the Prony series for both materials have quite different time constants. Since the creeping time we apply in the experiments is comparable to τ_1 , the pseudo-bistable behavior of the shells is also dominated by the relaxation over a time scale comparable to τ_1 . Therefore, in the following we only consider the first term in the Prony series.

Table 1. Viscoelastic properties of the silicone and urethane rubbers obtained by stress relaxation tests.

	μ ₀ (kPa)	g_1	τ_1 (s)	g_2	τ ₂ (s)
Dragon Skin TM 30 (D30)	281	0.0258	3.3870	0.0250	93.7974
VytaFlex TM 20 (V20)	172	0.2039	4.4193	0.1632	100.1317

Viscoelastic shells are fabricated by molding, and are bonded onto a hollow substrate made of polylactic acid (PLA), forming a shell unit, as shown in **Figure 3**a. To diminish the influence of geometric imperfections on the pseudo-bistability^[30], the molds for shells were 3D printed with high resolution (0.06 mm), and a step structure was used to ensure the concentricity between the shell and the substrate (Method, Figure S3-S5). We prepared the following four types of shell units: bistable shells and shells with zero, medium, and long recovery time. All the shells have the same radius R = 10 mm and height H = 4 mm. The thicknesses and materials for the shells of these four types are summarized in **Table 2**. The predicted recovery time for the shells with zero, medium and long recovery time by FEA is marked by a circle, square and pentagram in Figure 2e, respectively.

Table 2. Four types of shell units

Type	d/R	materials
Bistable shells	0.105	Dragon Skin TM 30 (D30)
Shells with $t_{rec} = 0$	0.125	Dragon Skin TM 30 (D30)
Shells with a medium t_{rec}	0.125	VytaFlex TM 20 (V20)
Shells with a long t_{rec}	0.115	VytaFlex TM 20 (V20)

Spatiotemporally programmable surfaces are created by assembling the shell units with different recovery time (Figure 3b and Figure S6). The shell units are interconnected via tubing so that the pressure loads exerted on them are always the same (Figure 3b and Figure S6). A pneumatic actuation system is used to extract, hold and release air (Figure 3b). This system contains three vacuum pumps connected in parallel, two 3-way solenoid valves, and a pressure sensor (Method and Figure S7). All the shell units are connected to this system in a way that

the tubing lengths from all the shell units to the pumps are equal (Figure S6b). Initially, the two solenoid valves are deactivated, and the pump can rapidly extract air from all the shell units, yielding a pressure load. Once the pressure reaches a targeted value, valve 2 is activated so that the pressure can be held. After a certain amount of creeping time t_{creep} , valve 1 is activated to release the pressure. As a result, the shells first buckle into the concave states at a critical pressure, and then start creeping during the pressure holding period (Figure 3c). After the pressure load is removed, different shells recover to their convex states at different predetermined recovery time t_{rec} , yielding spatiotemporal texture morphing (Figure 3c). With appropriate choices of shell units, we can create a surface with desired spatiotemporal textural morphing.

Next, we experimentally characterize the recovery time t_{rec} of shells on the spatiotemporally programmable surfaces. As an example, a surface is created by arranging the four types of shell units in a 4-by-3 grid pattern with each row corresponding to one type of shell units (Figure 3d and Figure S6), and is connected to the pneumatic actuation system. In each measurement, we fixed the average pressure load to be around 7 kPa during the holding process ($\Delta p/\mu_0 = 0.0249$ for D30, $\Delta p/\mu_0 = 0.0407$ for V20) (Figure S8), while changed the creeping time t_{creep} . We measured the average t_{rec} in five trials for $t_{creep} = 1$ s, 5 s, 10 s using a camera (Method). Using the middle shells in each row as examples, we find that t_{rec} for row 2 keeps nearly zero despite the increase in t_{creep} , whereas t_{rec} for row 3 and 4 increase with an increasing t_{creep} (blue solid lines in Figure 3e). Figure 3f summarizes the average t_{rec} for row 2, 3, and 4 when the surface is actuated for $t_{creep} = 10$ s (Movies S1), and compares the results with the corresponding numerical predictions. The experimental results show that the shells in row 2, 3, and 4 have almost zero, medium, and long t_{rec} , respectively, which agrees with the predictions from FEA. From Movie S1, we can clearly see that the shells in row 1 stay concave,

whereas the shells in row 2, 3, and 4 snap back sequentially after the pressure is released. To check whether t_{rec} of a shell in a surface is the same as that when it is actuated individually, we actuated the middle shells in row 2-4 individually, and measured t_{rec} for different t_{creep} (red dashed lines in Figure 3e). We find that the t_{rec} - t_{creep} curves only slightly shift down for the shells actuated individually. This is caused by the shorter time for air to flow into a single shell unit than that into the surface after the pressure is released, given that the surface has a chamber volume 12 times larger than a shell unit.

2.3 Surfaces exhibiting programmable temporal evolution of patterns

So far, we have identified via simulations and experiments four types of shell units: bistable shells and the shells with zero, medium and long recovery time t_{rec} . Next, we use these shell units as building blocks to create surfaces, which can display programmed patterns that evolve over time. To make the shells in the convex and concave states look more different, a piece of black thin paper with a hole is placed on the top of the shells (Figure S5). This cover is so flexible that it does not affect the snap motion of the shell. We first assembled 15 shell units into a 5-by-3 surface (**Figure 4a**), in which 2 shell units are bistable, 11 shell units have zero t_{rec} , 1 shell unit has medium t_{rec} , 1 shell unit has long t_{rec} . We instantaneously applied an average pressure around 7 kPa, held this pressure for $t_{creep} = 10$ s, and quickly released the pressure (similar to Figure 3d). At t = 0.33 s after the pressure is released, the shells with a zero t_{rec} snap from the concave state to the convex state, showing a digit number "5". At t = 2.57 s, the shell with a medium t_{rec} recovers, showing a digit number "6". At t = 9.33 s, the shell with a long t_{rec} recovers, showing a digit number "6". At t = 9.33 s, the shell with a long t_{rec} recovers, showing a digit number "6" have zero t_{rec} 2 shell units have long t_{rec} . We used the

same pressure load to actuate this new surface, and observed sequentially a smiley emoji at 0.30 s, a winking emoji at 2.97 s, and an astonished emoji at 11.03 s (Figure 4b and Movies S3).

2.4 Surfaces with programmable spatiotemporal friction

Besides displaying temporally programmable patterns, the surface can also exhibit spatiotemporal control of friction. When a single shell unit is in contact with a flat rigid plate, the friction at the interface depends on the convexity state of the shell. If the shell is concave, the plate is in contact with the PLA substrate, yielding a low friction. Otherwise, if the shell is convex, the friction is relatively high since the plate is in contact with the rubber (**Figure 5**b). Therefore, a surface comprising multiple shell units is capable of spatiotemporally tuning its friction by switching the states of the shell units.

We assembled a 4-by-3 surface composed of the four types of shell units. An acrylic board together with a weight (total weight 0.424 kg) was placed on this surface, and pulled forward at a constant velocity of 2 mm/s using an Instron testing machine (Model 5944) (Figure 5a, Figure S9). The effective frictional coefficient μ is given by the pulling force F divided by the normal force (4.16 N) exerted on the surface. While the board is pulled forward, the surface is subjected to a pressure load history in which an average pressure around 7 kPa is applied instantaneously, then held for $t_{creep} = 10$ s, and released (similar to that in Figure 3d). Accordingly, μ is high before the pressure load is applied when all the shell units are in the convex state. Then μ drops sharply and maintains low for $t_{creep} = 10$ s, since all the shells become concave due to the pressure load (Figure 5c). Depending on the types of the shell units in the surface, μ evolves quite differently over time after the pressure is released. When all the shell units have zero recovery time t_{ree} , they snap immediately after the pressure is released. Correspondingly, μ quickly recovers the value before the pressure load is applied (black line in Figure 5c). When all the shell units are bistable, they stay concave even though the pressure is

released. Thus, μ remains low (blue line in Figure 5c). When the surface is a mixture of the four types of shell units, where each row corresponds to one type (Figure S9a), μ exhibits a multistep function of time after the pressure is released (red line in Figure 5c), in which the first, second, and third steps correspond to the recovery of the shell units with zero, medium, and long $t_{\rm rec}$, respectively. Since the bistable shell units stay concave, the number of shell units in contact with the acrylic board is less than that before the pressure load is applied, and thus μ does not fully recover. We also find that the first step has a larger increase in μ than the other two steps, because the 3 shell units snapping back first bear the whole weight, leading to a larger contact area and thus a higher friction at the interface.

3. Conclusion

In summary, we propose a new design strategy for reconfigurable surfaces that can exhibit spatiotemporally programmable textural morphing with simple control. The surfaces are created by assembling an array of unit cells with tunable temporal responses, and can be reconfigured on demand by disassembling and reorganizing the unit cells. Here we adopt viscoelastic shells as the model unit cells, which can be pneumatically actuated to a concave state, and snap back to the convex state after a certain amount of time when the load is removed. Combining numerical simulations and experiments, we find that the recovery time of those shells can be broadly tuned by the geometry and viscoelastic property of the materials. Using the shell units with different recovery time, we create surfaces that can display pre-programmed temporal evolution of patterns, such as digit numbers and emoji. We also demonstrate that the surfaces can exhibit spatiotemporal evolution of friction.

The proposed spatiotemporally programmable surfaces open the door to a wide range of potential applications. For example, the surfaces could be employed as next-generation intelligent reflective roofs^[34]. The roof made of the surfaces can change its solar reflectance

over time by tuning its surface texture such that it reflects less light in the morning and evening, and more at noon. Besides, the surfaces could be programmed to have spatiotemporal wetting and adhesion properties^[35]. The surfaces could also be used to achieve spatiotemporally programmable electrical or thermal conductivity at interfaces by manipulating contact.

4. Methods

Finite element simulations

To investigate the behaviors of our viscoelastic shells in response to the pressure loads, we performed finite element analysis using the commercial software Abaqus/Standard. We first conducted the simulations for instantaneous loading. The incompressible Neo-hookean material was used to define hyperelastic behavior of the shells. Riks method was implemented to capture the complete equilibrium pressure-displacement responses. We then conducted simulations for time-dependent loading using dynamic implicit method. The single-term Prony series was used to describe the viscous behavior of the shells. Numerical damping with moderate dissipation was applied to reduce the noise to the solution caused by the rapid snap motion. In all the simulations, we constructed axisymmetric shell models and meshed them using hybrid quadratic rectangular elements (Abaqus type CAX8H). We imposed a fixed boundary condition on the edge of the shells.

Stress relaxation tests

Stress relaxation tests were performed to determine the viscoelastic properties of the silicone rubber (Dragon SkinTM30) and urethane rubber (VytaFlexTM 20). A thin film specimen of length 80 mm, width 20 mm, and thickness 2 mm was fabricated by molding for each material, with 1% by weight of IgniteTM orange pigment. An Instron testing machine (Model 5944) equipped with a 50 N loading cells was used for the tests. In the relaxation tests, a 20% tensile strain was applied within 0.5 s and maintained for 300 s. The relations between the resultant forces and time were recorded. A two-term Prony series was fitted to the experimental data

using the least-square approach to determine the viscoelastic properties of the materials. We find that the two-term Prony series is sufficient for an accurate fit (the root-mean-square error is less than 0.6%). More details on curve fitting are provided in Supplementary Text 1.

Fabrication of viscoelastic shell units

The shells are made of silicone rubber (Dragon SkinTM30) and urethane rubber (VytaFlexTM 20), with 1% by weight IgniteTM orange pigment. We casted the materials into PLA two-part molds, which were printed by a Ultimaker S5 printer with resolution (layer height) 0.06 mm. The inner surfaces of the molds for urethane shells were coated with UniversalTM Mold Release to facilitate demolding. All the shells have a radius R = 10 mm and height H = 4mm. Their thickness d is varied from 1.05 mm to 1.25 mm. The shells at their edges have a flange of width 3 mm. The change in volume of a shell from its concave state to convex state is 528.66 mm³ when d = 1.05 mm and 492.82 mm³ when d = 1.25 mm. After the shells are made, they were glued onto a hollow substrate by applying super glues onto the flanges of the shells. The substrate was made of PLA and 3d-printed in the same way as the molds. The chamber in the substrate is a cylindrical void of radius 10 mm and height 34 mm, yielding a volume 10681 mm³. The change in volume caused by the snap motion is less than 5% of the volume of the chamber, and thus, the snapping of one shell does not influence the recovery of others. More details on the fabrication of the shell units are provided in Supporting Information. Pneumatic actuation system

A pneumatic actuation system was built for extracting air from the shell units, and holding and releasing the pressure. This system consists of three vacuum pumps connecting in parallel (2.1 L/min), two 3-way miniature solenoid valves, an Arduino microcontroller, a power supply, and a pressure sensor (Panasonic, ADP5101) (Figure S7). We used a camera (Sony

Alpha a6000, 60fps) to record the snap motion of the shells. When the pressure is released, a 5 mm LED red lamp is turned on to start timing.

Supporting Information

Supporting Information is available from the Wiley Online Library or from the author.

Acknowledgements

This work is supported by the startup fund from Henry Samueli School of Engineering and Applied Science at the University of California, Los Angeles (UCLA), and National Science Foundation through a CAREER Award No. CMMI-2048219. This work used computational and storage services associated with the Hoffman2 Shared Cluster provided by UCLA Institute for Digital Research and Education's Research Technology Group.

Received: ((will be filled in by the editorial staff))

Revised: ((will be filled in by the editorial staff))

Published online: ((will be filled in by the editorial staff))

References

- [1] H. Marvi, J. P. Cook, J. L. Streator, D. L. Hu, Biotribology 2016, 5, 52.
- [2] R. Hanlon, Curr. Biol. 2007, 17, R400.
- [3] J. J. Allen, G. R. R. Bell, A. M. Kuzirian, S. S. Velankar, R. T. Hanlon, *J. Morphol.* **2014**, 275, 371.
- [4] I. Dayyani, A. D. Shaw, E. I. Saavedra Flores, M. I. Friswell, *Compos. Struct.* **2015**, *133*, 358.
- [5] D. Li, S. Zhao, A. Da Ronch, J. Xiang, J. Drofelnik, Y. Li, L. Zhang, Y. Wu, M. Kintscher, H. P. Monner, A. Rudenko, S. Guo, W. Yin, J. Kirn, S. Storm, R. D. Breuker, *Prog. Aerosp. Sci.* 2018, 100, 46.
- [6] J. Rossignac, M. Allen, W. J. Book, A. Glezer, I. Ebert-Uphoff, C. Shaw, D. Rosen, S. Askins, Jing Bai, P. Bosscher, J. Gargus, Byung Moon Kim, I. Llamas, A. Nguyen, Guang Yuan, Haihong Zhu, in *2003 Shape Model. Int.*, IEEE Comput. Soc, Seoul, South Korea, **2003**, pp. 229–231.
- [7] A. A. Stanley, K. Hata, A. M. Okamura, in 2016 IEEE Int. Conf. Robot. Autom. ICRA, IEEE, Stockholm, Sweden, 2016, pp. 2718–2724.
- [8] Y. Hu, Z. Zhao, A. Vimal, G. Hoffman, in 2018 IEEE Int. Conf. Soft Robot. RoboSoft, IEEE, Livorno, 2018, pp. 182–187.
- [9] J. H. Pikul, S. Li, H. Bai, R. T. Hanlon, I. Cohen, R. F. Shepherd, Science 2017, 358, 210.

- [10] A. Rafsanjani, Y. Zhang, B. Liu, S. M. Rubinstein, K. Bertoldi, Sci. Robot. 2018, 3, eaar7555.
- [11] C. Lamuta, H. He, K. Zhang, M. Rogalski, N. Sottos, S. Tawfick, *Adv. Mater. Technol.* **2019**, *4*, 1900260.
- [12] Y. Wang, H. Cui, Q. Zhao, X. Du, *Matter* **2019**, *1*, 626.
- [13] F. Fei, P. Kotak, L. He, X. Li, C. Vanderhoef, C. Lamuta, X. Song, *Adv. Funct. Mater.* **2021**, 2105528.
- [14] K. Liu, F. Hacker, C. Daraio, Sci. Robot. 2021, 6, eabf5116.
- [15] Y. Alapan, A. C. Karacakol, S. N. Guzelhan, I. Isik, M. Sitti, Sci. Adv. 2020, 6, eabc6414.
- [16] Y. Zhang, Z. Yan, K. Nan, D. Xiao, Y. Liu, H. Luan, H. Fu, X. Wang, Q. Yang, J. Wang, W. Ren, H. Si, F. Liu, L. Yang, H. Li, J. Wang, X. Guo, H. Luo, L. Wang, Y. Huang, J. A. Rogers, *Proc. Natl. Acad. Sci.* 2015, 112, 11757.
- [17] M. A. Dias, M. P. McCarron, D. Rayneau-Kirkhope, P. Z. Hanakata, D. K. Campbell, H. S. Park, D. P. Holmes, *Soft Matter* **2017**, *13*, 9087.
- [18] P. Celli, C. McMahan, B. Ramirez, A. Bauhofer, C. Naify, D. Hofmann, B. Audoly, C. Daraio, *Soft Matter* **2018**, *14*, 9744.
- [19] Y. Park, G. Vella, K. J. Loh, Sci. Rep. 2019, 9, 18609.
- [20] E. Siéfert, E. Reyssat, J. Bico, B. Roman, Nat. Mater. 2019, 18, 24.
- [21] R. Guseinov, C. McMahan, J. Pérez, C. Daraio, B. Bickel, Nat. Commun. 2020, 11, 237.
- [22] A. Nojoomi, H. Arslan, K. Lee, K. Yum, *Nat. Commun.* **2018**, *9*, 3705.
- [23] J. W. Boley, W. M. van Rees, C. Lissandrello, M. N. Horenstein, R. L. Truby, A. Kotikian, J. A. Lewis, L. Mahadevan, *Proc. Natl. Acad. Sci.* **2019**, *116*, 20856.
- [24] A. A. Bauhofer, S. Krödel, J. Rys, O. R. Bilal, A. Constantinescu, C. Daraio, *Adv. Mater.* **2017**, *29*, 1703024.
- [25] E. Hajiesmaili, D. R. Clarke, Nat. Commun. 2019, 10, 183.
- [26] T. Chen, O. R. Bilal, K. Shea, C. Daraio, *Proc. Natl. Acad. Sci.* **2018**, *115*, 5698.
- [27] Y. Liu, B. Shaw, M. D. Dickey, J. Genzer, Sci. Adv. 2017, 3, e1602417.
- [28] Y. Mao, K. Yu, M. S. Isakov, J. Wu, M. L. Dunn, H. Jerry Qi, Sci. Rep. 2015, 5, 13616.
- [29] T. Liu, Y. Chen, L. Liu, Y. Liu, J. Leng, J. Hutchinson, L. Jin, **2021**.
- [30] T. Liu, Y. Chen, L. Liu, Y. Liu, J. Leng, L. Jin, Extreme Mech. Lett. **2021**, 49, 101477.
- [31] A. Brinkmeyer, M. Santer, A. Pirrera, P. M. Weaver, Int. J. Solids Struct. 2012, 49, 1077.
- [32] M. Gomez, D. E. Moulton, D. Vella, J. Mech. Phys. Solids 2019, 124, 781.
- [33] E. Y. Urbach, E. Efrati, Sci. Adv. 2020, 6, eabb2948.
- [34] A. L. Pisello, Sol. Energy **2017**, 144, 660.
- [35] M. Liu, S. Wang, L. Jiang, *Nat. Rev. Mater.* **2017**, *2*, 17036.

Figures

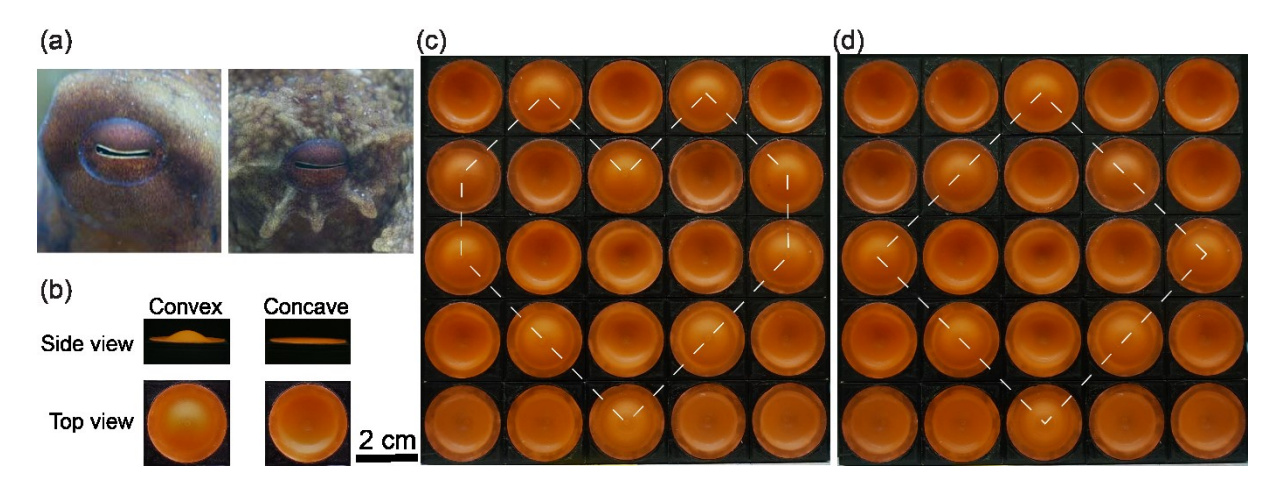


Figure 1. Spatiotemporally programmable surfaces inspired by the skin papillae in cephalopods. (a) Cephalopods can alter their appearance for camouflage by changing the morphology of their skin papillae. Reproduced with permission. [3] Copyright 2013, Wiley Periodicals, Inc. (b) As the unit cell of the surfaces, a viscoelastic shell can have two states: convex and concave, analogous to the extended and retracted states of the papillae of cephalopods. The convex shell can be pneumatically actuated to the concave state, and recover the initial convex state after a certain amount of time when the load is removed. (c-d) By arranging the shells of different recovery time, surfaces can be formed to exhibit pre-programmed spatiotemporal textural morphing. The surfaces can be easily disassembled and rearranged to new ones with different spatiotemporal responses. A "heart" texture shown in (c) can be reconfigured into a "tilted square" texture in (d) by simply reorganizing the shell units.

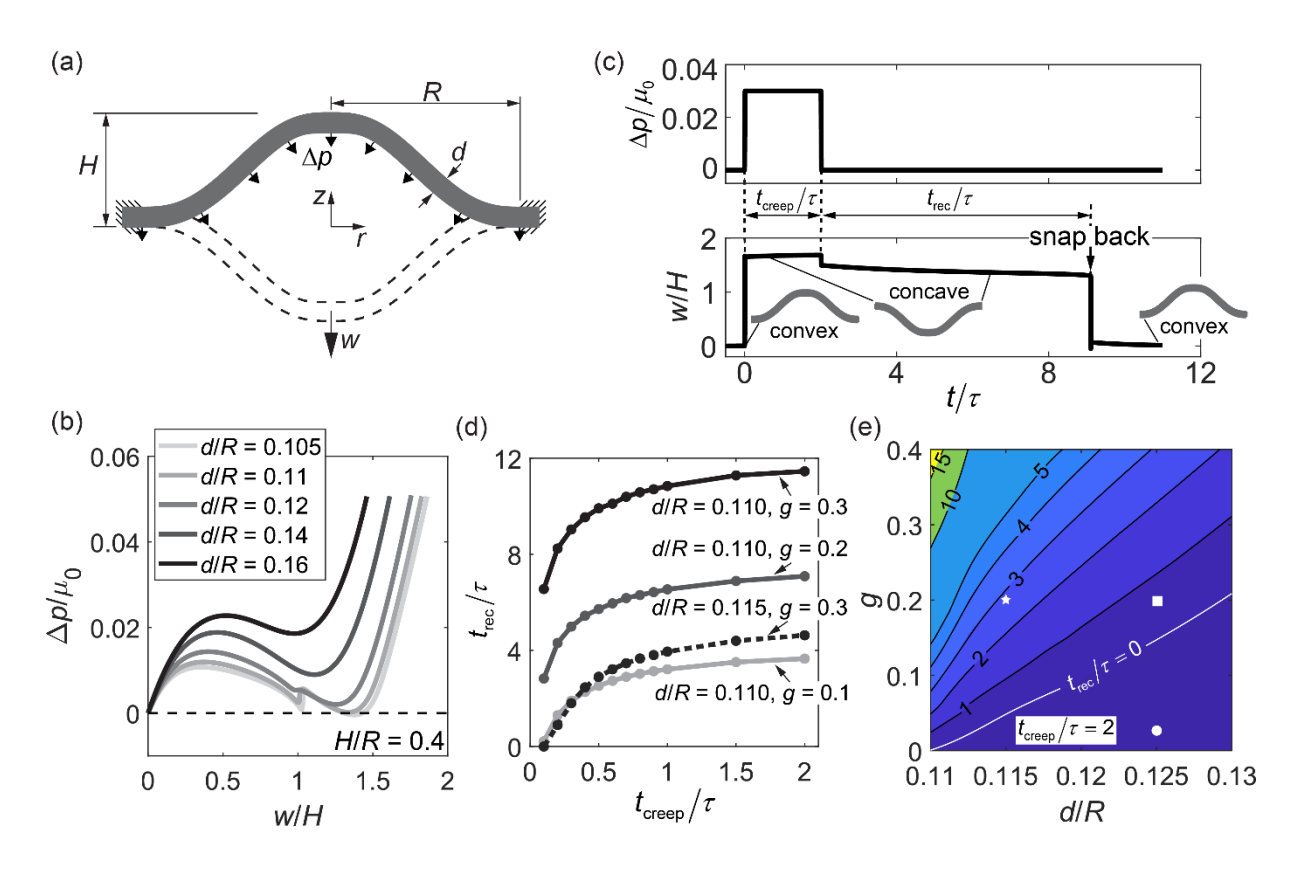


Figure 2. Numerical study of viscoelastic shells with tunable recovery time. (a) Geometry of the shells. The shell is defined by its thickness d, radius R, and height H. The shell can buckle into a concave shape (dashed lines) under a pressure load Δp , yielding a displacement w at its center. (b) The normalized pressure-displacement relations for the shells with H/R = 0.4 and different d/R ranging from 0.105 to 0.16 under instantaneous loading. The curves intersecting $\Delta p/\mu = 0$ (dashed line) correspond to bistable shells. (c) Applied pressure-time relation and the corresponding evolution of the displacement over time for the shell with d/R = 0.11, H/R = 0.4, and g = 0.2. The time period when a constant pressure is held is defined as the creeping time $t_{\rm creep}$, while the time period when the shell stays concave after the pressure is removed is defined as recovery time $t_{\rm rec}$, which are both normalized by the relaxation time constant of the viscoelastic material τ . (d) The effect of $t_{\rm creep}/\tau$, d/R, and dimensionless relaxation modulus g on $t_{\rm rec}/\tau$ (e) Contour of $t_{\rm rec}/\tau$ with respect to g and d/R when $t_{\rm creep}/\tau = 2$. The area underneath the white line corresponds to zero recovery time. The circular, square and pentagram white markers

represent the predictions for the viscoelastic shells with zero, intermediate, and long recovery time in the experiments, respectively.

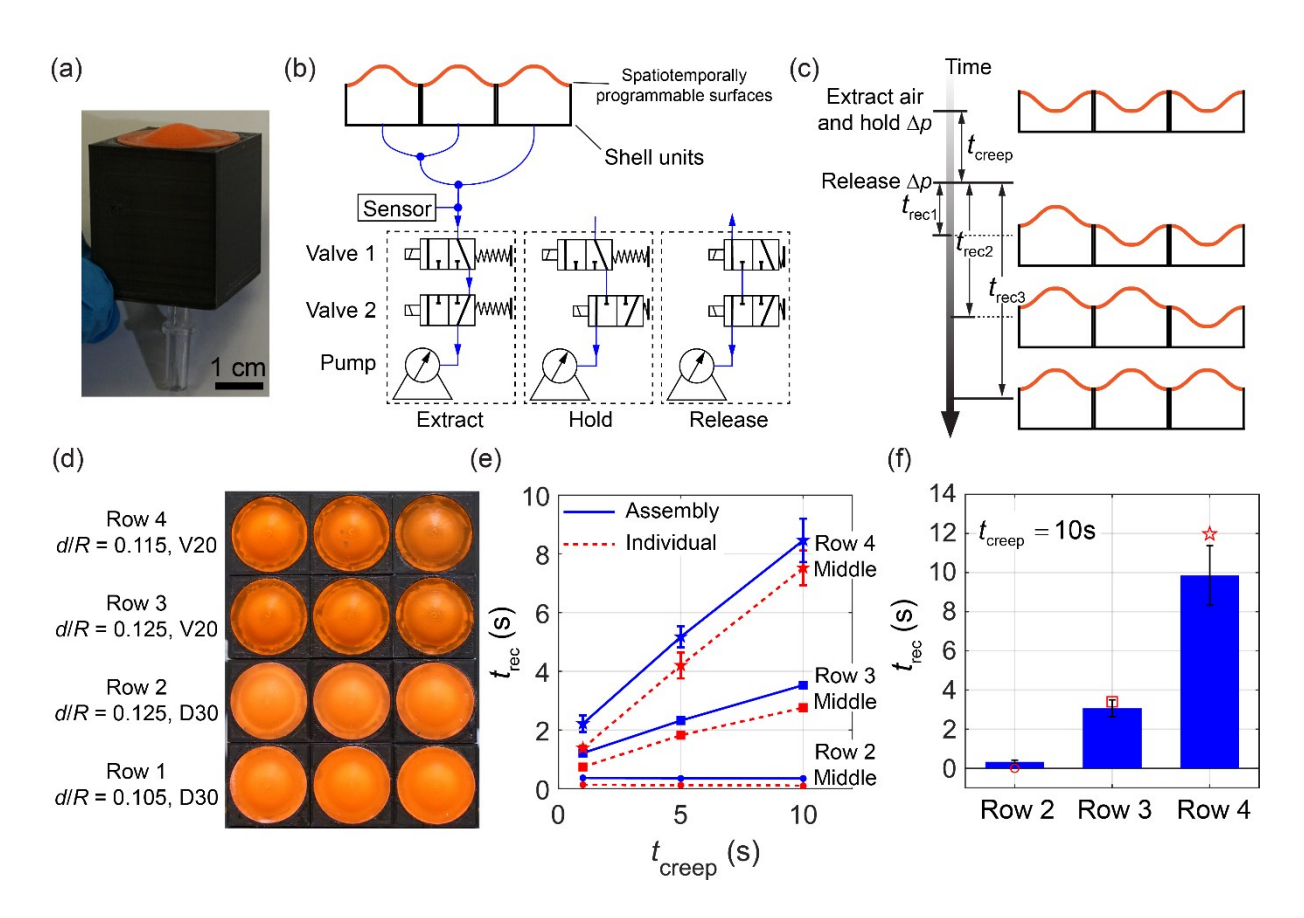


Figure 3. Spatiotemporally programmable surfaces and experimental characterization. (a) Snapshot of a shell unit comprising a viscoelastic shell bonded to a hollow substrate made of PLA. (b) Schematic of a spatiotemporally programmable surface and a pneumatic actuation system for extracting, holding and releasing air, where the blue lines represent air flow. (c) Schematic of the principle for a surface exhibiting pre-programmed spatiotemporal textural morphing under simple pneumatic actuation. When a pressure Δp is applied, the convex shells buckle into the concave states. The pressure is then held for t_{creep} , followed by being released. As a result, the shells snap back to the convex state at different predetermined recovery time t_{ree} , yielding temporal texture evolution. (d-f) Experimental characterization. (d) A surface with 12 shell elements arranged in 4 rows and 3 columns; each row corresponds to one type of shells with different geometry or materials from those in other rows. The shells in row 1 and 2 are made of Dragon SkinTM 30 (D30), and the shells in row 3 and 4 are made of VytaFlexTM 20 (V20). The shells in row 1 are bistable, while the shells in row 2, 3, and 4 have zero, medium,

and long recovery time, respectively. (e) The dependence of the recovery time t_{rec} on the creeping time t_{creep} . The blue solid lines represent the results of a shell when it is actuated within the surface in (d), whereas the red dashed lines represent the results when the same shell is actuated individually. (f) Histogram of the average t_{rec} in each row of the surface when $t_{creep} = 10$ s. The red hollow markers represent the numerical predictions obtained from Figure 2e. The error bars indicate the standard deviations of the measurements.

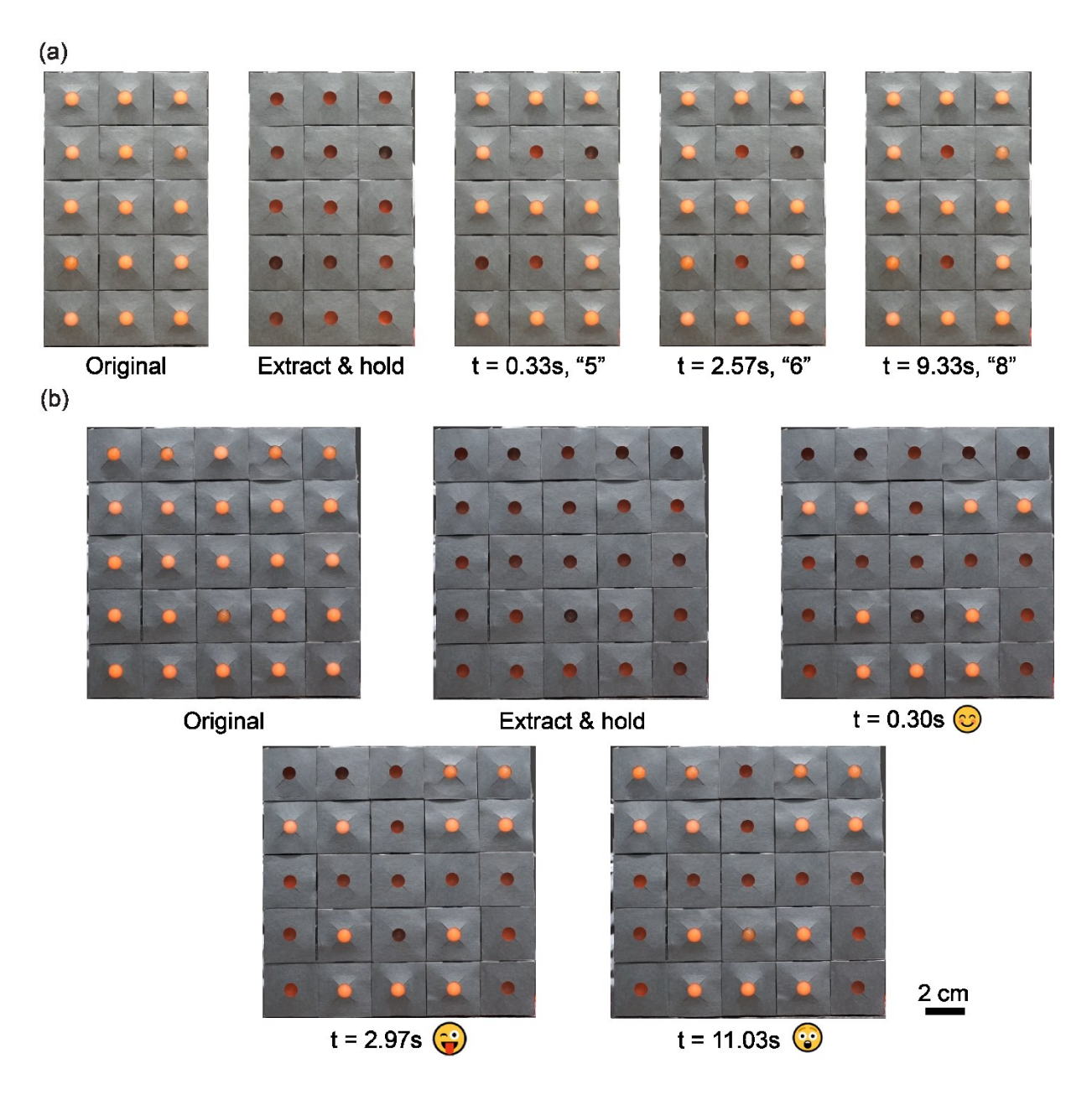


Figure 4. Surfaces exhibiting temporal evolutions of patterns. (a) The surface shows sequentially a digit number "5" at 0.33 s, "6" at 2.57 s, and "8" at 9.33 s. (b) Another surface displays different emoji in order of time: a smiley emoji at 0.30 s, a winking emoji at 2.97 s, and an astonished emoji at 11.03 s.

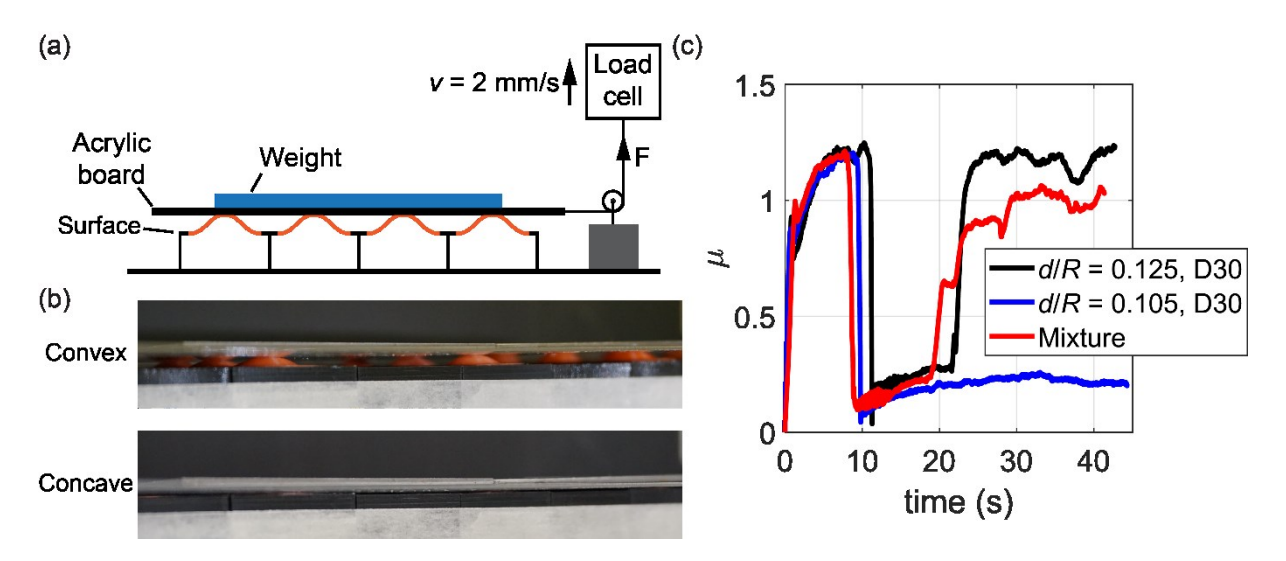


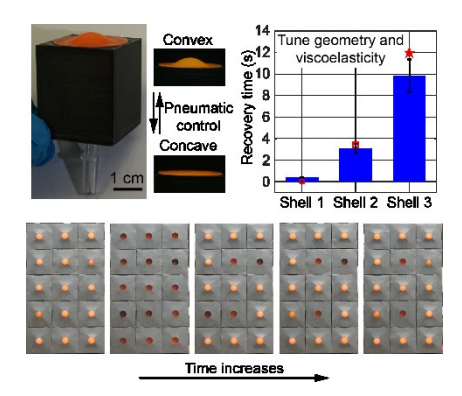
Figure 5. Surfaces with programmable spatiotemporal friction. (a) Schematic of the experimental setup to measure the effective frictional coefficient between an acrylic board and a surface. The acrylic board together with a weight is placed on the surface. The load cell pulls the acrylic board at a constant velocity v = 2 mm/s and records the resultant pulling force F. (b) When the shells are convex (top), the acrylic board contacts the rubber shells, yielding high friction. When the shells are concave (bottom), the acrylic board contacts the PLA substrate, yielding low friction. When the convexity of the shells spatiotemporally evolves, the frictional property of the surface also varies. (c) The effective frictional coefficients μ as functions of time for surfaces with 12 shell units arranged in 4 rows and 3 columns. The black and blue solid lines represent the surfaces in which all the 12 shell units have zero recovery time, and are bistable, respectively. The red solid line represents the one with a mixture of bistable shells and shells with zero, medium and long recovery time.

Table of Contents

A design strategy for reconfigurable surfaces exhibiting spatiotemporally programmable textural morphing under simple control is proposed. Viscoelastic shells that can temporarily stay concave before recovering the initial convex state without external loads are chosen as unit cells. Integrating such shells with broadly tuned recovery time by geometry and material viscoelasticity, we create surfaces exhibiting spatiotemporal evolution of patterns and friction.

Yuzhen Chen, Tianzhen Liu, and Lihua Jin*

Title: Spatiotemporally programmable surfaces via viscoelastic shell snapping



Supporting Information

Title Spatiotemporally programmable surfaces via viscoelastic shell snapping

Yuzhen Chen, Tianzhen Liu, and Lihua Jin*

Supplementary Text 1: Material modeling and characterization

We used the following incompressible neo-Hookean material model to define the instantaneous constitutive behavior of the shells,

$$W = \frac{\mu}{2} \left[\text{tr}(\mathbf{F}\mathbf{F}^{T}) - 3 \right], \tag{S1}$$

where W is the strain energy density function, μ is the shear modulus, F is the deformation gradient tensor. To describe the viscoelastic behavior of the shells, Prony series were used and the shear modulus μ can be expressed as

$$\mu(t) = \mu_0 \left[1 - \sum_{i=1}^n g_i \left(1 - e^{-t/\tau_i} \right) \right], \tag{S2}$$

where μ_0 is the instantaneous shear modulus, n is the number of the series terms, g_i is the dimensionless relaxation modulus, t is the time, and τ_i is the relaxation time constant.

Here we characterize the viscoelastic properties of the silicone rubber (Dragon SkinTM30) and urethane rubber (VytaFlexTM 20). We modeled their viscous part as two-term Prony series (n = 2 in Eq. S2). Combining Eq. S1 and S2, the nominal (first Piola-Kirchoff) stress under uniaxial tension is then given by

$$S_{11} = \mu(t) \left(\lambda - \frac{1}{\lambda^2} \right), \tag{S3}$$

where S_{11} and λ represent the nominal stress and stretch along the loading direction, respectively, $\mu(t)$ is the shear modulus at time t,

$$\mu(t) = \mu_0 \left[1 - g_1 \left(1 - e^{-t/\tau_1} \right) - g_2 \left(1 - e^{-t/\tau_2} \right) \right]. \tag{S4}$$

During the stress relaxation tests, $\lambda = 1.2$ was applied instantaneously, and S_{11} decaying as a function of time was measured. Substituting the measured S_{11} into Eq. S3 to obtain the $\mu - t$ relation, and fitting Eq. S4 to the experimental data using the linear least-square method, we obtained μ_0 , g_1 , τ_1 , g_2 , τ_2 for the two materials, as shown in Table 1. In Figure S1, we can see that the two-term Prony series are sufficient for an accurate fit (the root-mean-square error is less than 0.6%).

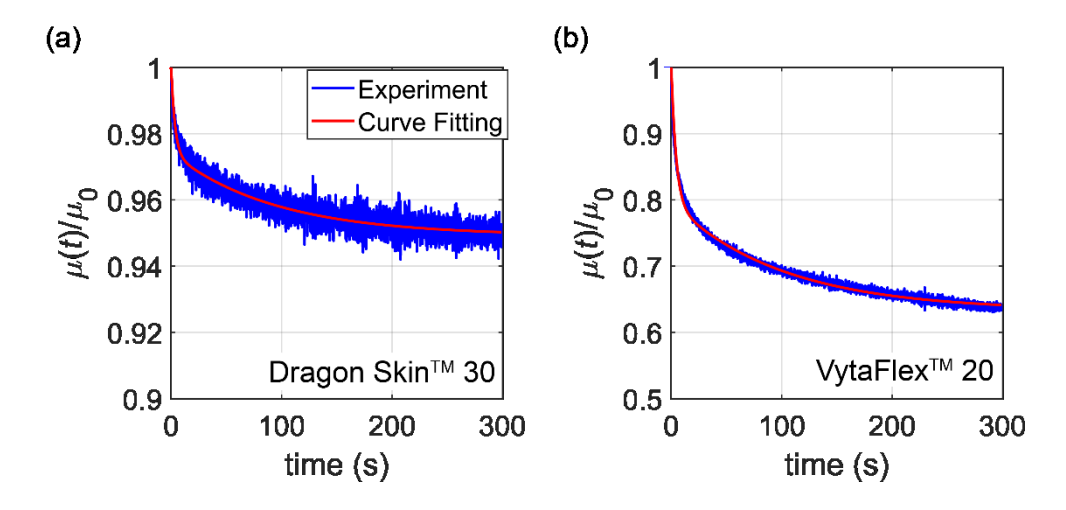


Figure S1. Characterization of the viscoelastic properties for the silicone rubber (Dragon SkinTM30) and urethane rubber (VytaFlexTM 20). (a-b) The evolution of the normalized shear modulus over time, $\mu(t)$, during the stress relaxation tests for Dragon SkinTM 30 (a) and VytaFlexTM 20 (b). The blue curves represent the experimental data, while the red curves represent the curve fitting.

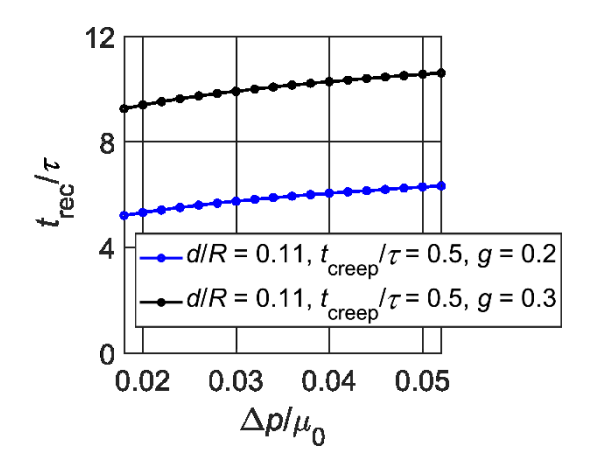


Figure S2. Pressure $\Delta p/\mu_0$ has a small effect on the recovery time $t_{\rm rec}/\tau$. The shells with H/R = 0.4, d/R = 0.11, g = 0.2 (blue curve) or 0.3 (black curve) are subjected to a constant pressure $\Delta p/\mu_0$ for $t_{\rm creep}/\tau = 0.5$ prior to its releasing. As $\Delta p/\mu_0$ increases from 0.02 to 0.05, $t_{\rm rec}/\tau$ only increases by 18.20% (g = 0.2) and 12.34% (g = 0.3).

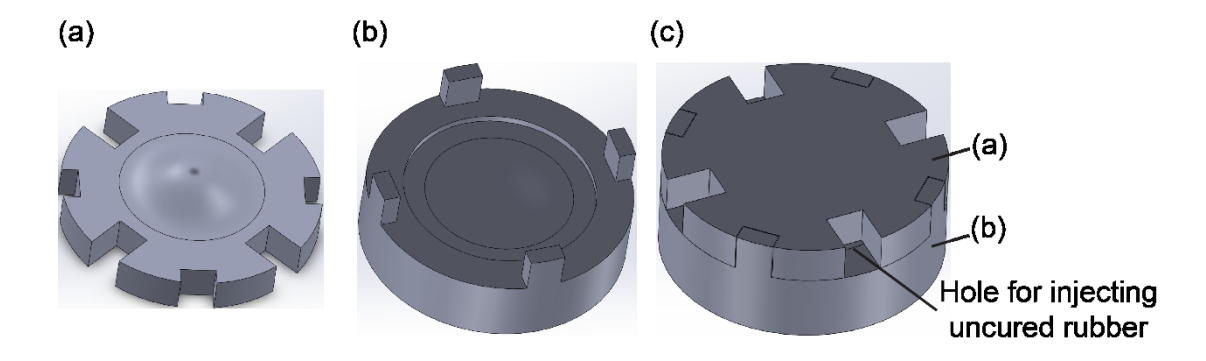


Figure S3. The 3D model of the two-part mold for fabricating viscoelastic shells. This mold (c) consists of the upper part (a) and lower part (b). The uncured rubber is injected into the mold through any one of the four holes on the mold.

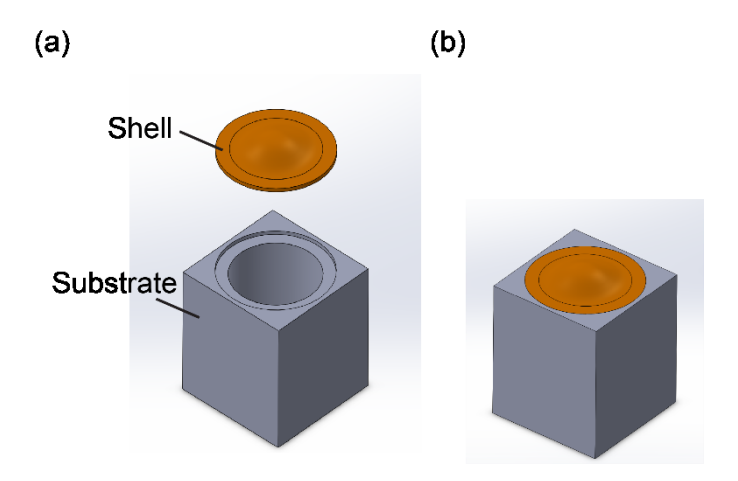


Figure S4. The assembly of the shell and the substrate. (a) The 3D model of the substrate. The substrate has a cylindrical chamber with radius 10 mm and height 34 mm. It also has a step structure with the same width (3 mm) as the flange of the shell. (b) The shell is bonded onto the substrate by applying super glues onto its flange. The step structure on the substrate can guarantee the concentricity between the shell and the substrate.

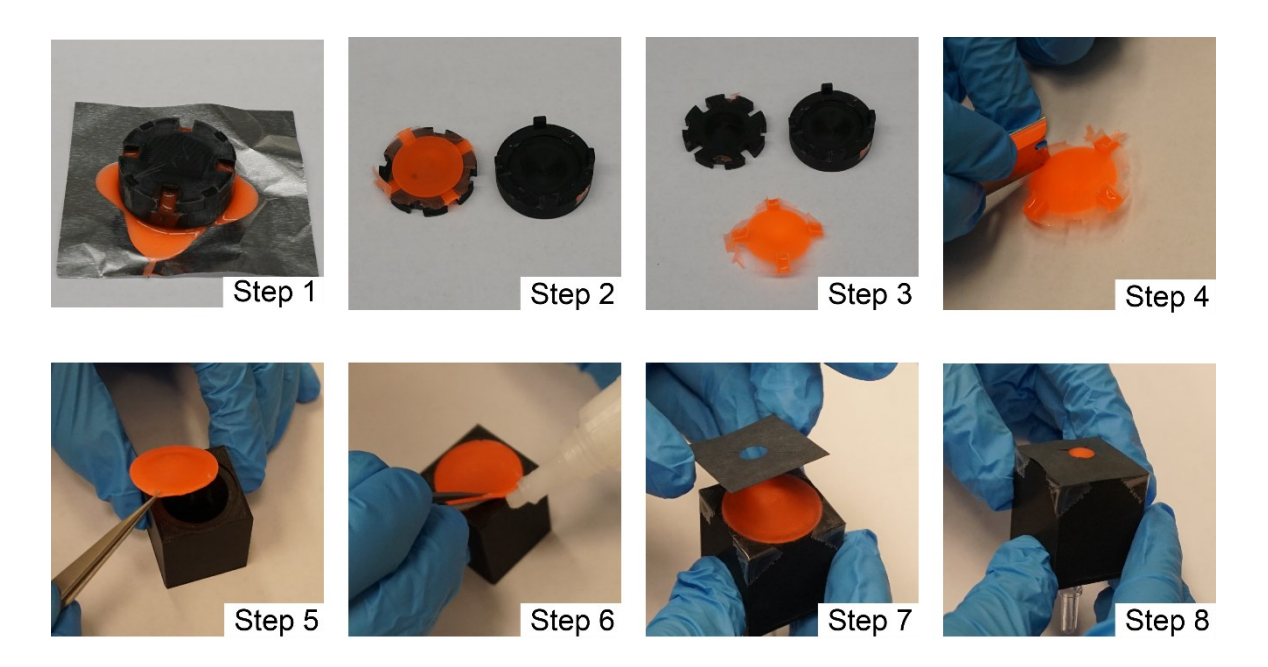


Figure S5. The fabrication procedure of a shell unit. Step 1, inject uncured rubber into the mold through the holes on the mold using syringes. Step 2, open the mold after the rubber is fully cured. Step 3, peel off the shell. Step 4, cut the excessive parts from the shell. Step 5, place and

align the shell on the top of the hollow substrate. Step 6, glue the flange part of the shell onto the substrate. Step 7, when needed, align a flexible black paper with a hole at its center with the shell. Step 8, bond the paper on the substrate via double-sided tapes.

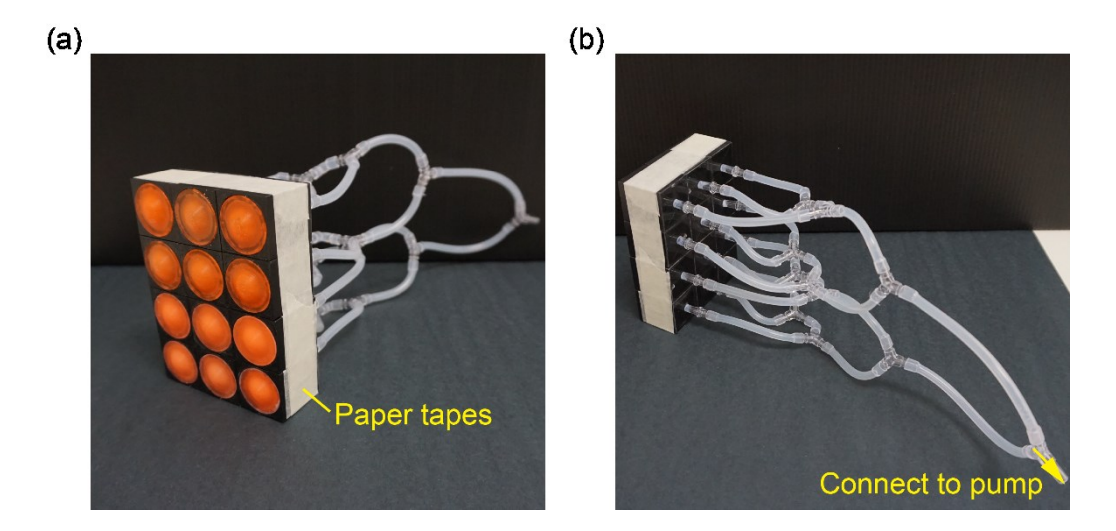


Figure S6. Surface and its tubing. (a) Oblique view of the surface. The surface is created by aligning and binding the shell units together by paper tapes. (b) Back view of the surface. The shell units are interconnected via silicone tubing in a way that the shell units have equal distances to the vacuum pump.

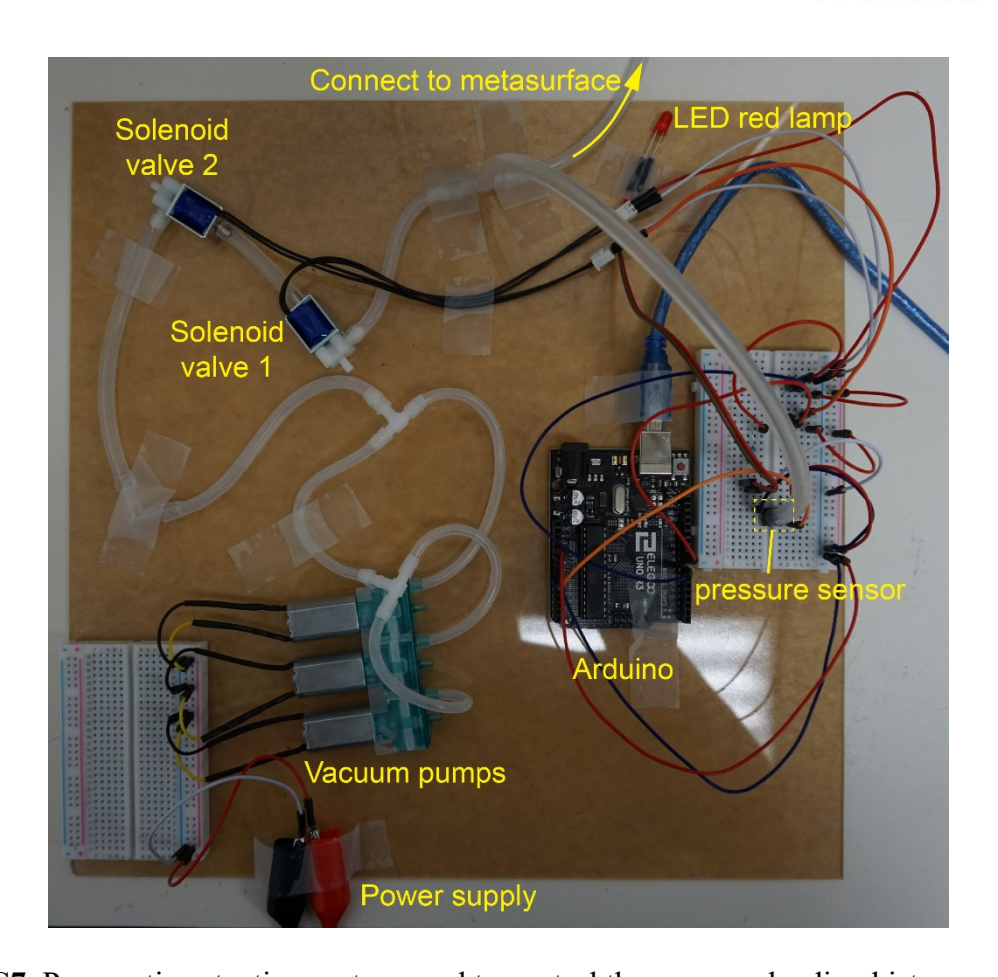


Figure S7. Pneumatic actuation system used to control the pressure loading history.

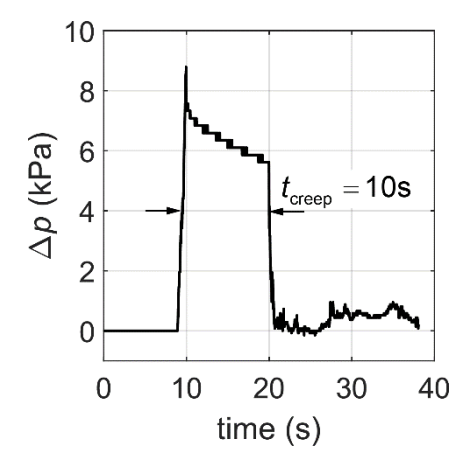


Figure S8. Evolution of the measured pressure over time. The surface in Figure 3d is connected to the pneumatic actuation system (Figure S7), and is subjected to an average pressure load 7 kPa ($\Delta p/\mu_0 = 0.0249$ for D30, $\Delta p/\mu_0 = 0.0407$ for V20) for $t_{\text{creep}} = 10$ s. Due to slight leakage, the pressure during the holding process decays. To achieve an average pressure load 7 kPa, initially a pressure 8.59 kPa is applied, and the pressure decays to 5.52 kPa after $t_{\text{creep}} = 10$ s

 $(\Delta p/\mu_0)$ reduces from 0.0306 to 0.0196 for D30, from 0.0499 to 0.0321 for V20), yielding an average pressure load around 7 kPa. Despite the time-varying pressure, the recovery time t_{rec} of each shell unit can still be well-controlled, since t_{rec} is not sensitive to the applied pressure (Figure S2).

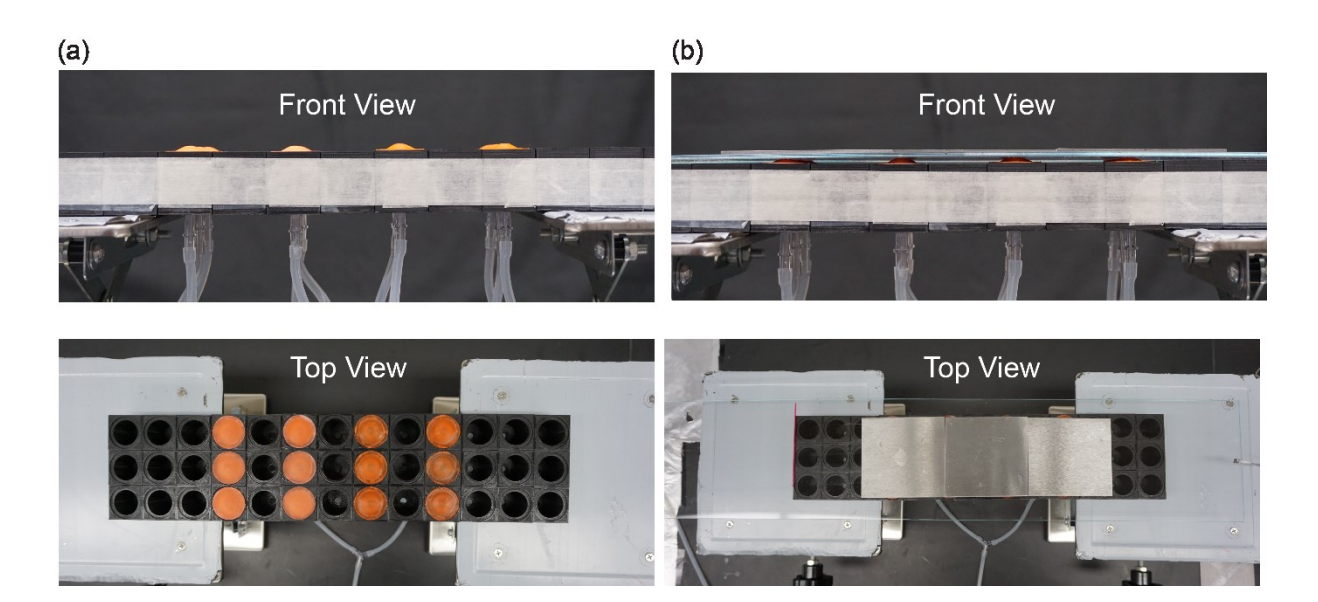


Figure S9. Experimental setup for measuring the effective frictional coefficients between an acrylic board and a surface. (a) Front and top view of a surface with a mixture of the four types of shell units. From left to right: bistable shell units, the shell units with zero, medium, and long recovery time. (b) Front and top view of the surface when an acrylic board together with a weight is placed on it.

Movie S1. Surface composed of viscoelastic shells with different recovery time in each row

Movie S2. Surface displaying temporal evolution of digit numbers

Movie S3. Surface displaying temporal evolution of emoji